



## Full Text View

[Volume 29, Issue 7 \(July 1999\)](#)

### Journal of Physical Oceanography

Article: pp. 1579–1598 | [Abstract](#) | [PDF \(581K\)](#)

# A Three-Dimensional Simulation of the Formation of Anticyclonic Lenses (Meddies) by the Instability of an Intermediate Depth Boundary Current

**Johann H. Jungclaus\***

*Program in Atmospheric and Oceanic Sciences, Princeton University, Princeton, New Jersey*

(Manuscript received February 4, 1997, in final form August 20, 1998)

DOI: 10.1175/1520-0485(1999)029<1579:ATDSOT>2.0.CO;2

## ABSTRACT

The evolution of a buoyancy-driven intermediate water current along an idealized continental slope is investigated using a three-dimensional primitive equation ocean model. The outflow current, originating in a marginal sea, flows northward along a linear sloping bottom where it undergoes considerable mixing. For a parameter range resembling the Mediterranean outflow, the flow becomes hydrodynamically unstable. The intruding, relatively dense outflow water interacts with the overlaying slope water by inducing vortex compression and stretching. The phase relation between the upper-layer and lower-layer perturbations indicates that baroclinic instability is the driving mechanism in the initial destabilization. As the disturbances grow to large amplitude, dipoles are formed and move away from the boundary current in a westward direction. While the amplifying anticyclones wrap around the intruding low potential vorticity water, the cyclones usually entrain ambient water and decrease in strength. Isolated anticyclones finally separate from the boundary current and develop a southward translation component. In some cases dipolar structures remain intact and propagate to the west. In the slope water strong cyclones and somewhat weaker anticyclones are formed periodically and travel in the direction of the bottom flow. The upper-layer flow shows surface expressions of the middepth lenses that develop as meddies. These penetrate into the ambient slope water and gain a barotropic velocity component. The adjustment process is discussed in terms of potential vorticity conservation.

The instability mechanism discussed here does not require any topographic irregularities. Sensitivity experiments, however, suggest that canyons or capes introduce an additional source of vorticity and may lead to the observed localization of spawning events.

### Table of Contents:

- [Introduction](#)
- [The numerical model](#)
- [The standard experiment](#)
- [Sensitivity studies](#)
- [Summary and discussion](#)
- [REFERENCES](#)
- [APPENDIX](#)
- [FIGURES](#)

### Options:

- [Create Reference](#)
- [Email this Article](#)
- [Add to MyArchive](#)
- [Search AMS Glossary](#)

### Search CrossRef for:

- [Articles Citing This Article](#)

### Search Google Scholar for:

- [Johann H. Jungclaus](#)

## 1. Introduction

Bottom-water formation takes place mainly in marginal seas and on the shelves of high-latitude oceans. The densest water fills the deep layers of the marginal seas or shallow embankments on the shelf. Eventually, the dense water spills over the shelf break and finds its way into the deep and intermediate layers of the ocean in the form of a bottom vein or gravity current. During the descent of often more than 1 or 2 km (where the downslope movement is accomplished by Ekman transport and by baroclinic eddies) it entrains a considerable amount of the surrounding waters, and its final depth level in the ocean is determined by the relative density contrast between the plume and the ambient waters.

In a study of the major outflows contributing to the deep waters of the North Atlantic, [Price and Baringer \(1994\)](#) compared the respective pathways and water mass transformations. The Mediterranean outflow possesses the densest source water ( $S = 38.45$  psu;  $T = 13.0^\circ\text{C}$ ;  $\sigma_\theta = 28.95$  kg m<sup>-3</sup>), but, on the other hand, undergoes the most vigorous mixing.

In contrast to the high-latitude outflows, it loses most of its density contrast of initially about 1.5 kg m<sup>-3</sup> by the time the outflow water reaches the southwestern corner of Portugal at Cape St. Vincent. More detailed hydrographic observations (e.g., [Zenk and Armi 1990](#); [Daniault et al. 1994](#)) reveal that the upper part of the outflow continues to follow the western European continental slope far northward in the form of a bottom boundary current centered at about 600 m. The lower core detaches from the bottom to the west of Portugal and near Cape St. Vincent. Submesoscale eddies (meddies) pinch off from the outflow and transport their salt and heat content in a mainly southwestward direction, thus accounting for a large portion of the observed large-scale diffusive exchange between the Mediterranean Water (MW) and the intermediate Atlantic waters ([Arhan and King 1995](#)). Meddies typically show temperature and salinity anomalies of 1°–2.5°C and 0.4–0.8 psu, respectively ([Armi and Zenk 1984](#)). The inner core of a meddy is in almost solid-body rotation with azimuthal velocities of 10–30 cm s<sup>-1</sup> and a relative vorticity of typical  $-0.4f$ , but as negative as  $-0.85f$  are observed ([Prater and Sanford 1994](#)). The vertical extent of the lenses is about 600–1000 m and typical diameters are 20–100 km. Since the interior anomalies are shielded from the ambient waters by a pronounced potential vorticity front, meddies decay only slowly. They often travel long distances without losing their characteristic temperature and salinity anomaly ([Armi et al. 1989](#)).

There are several generation mechanisms discussed in the literature, and [Prater \(1992\)](#) reviewed the relevant theories in his discussion of a meddy found in the Gulf of Cadiz. Several authors point to the vorticity generation at capes or canyons. [D'Asaro \(1988\)](#) suggests that anticyclonic vorticity can be induced in a flow following a coastline on its right side by boundary torque. When the flow separates from the boundary at a cape or upon exiting a canyon, anticyclonic eddies form. D'Asaro used this theory to explain the predominance of anticyclones in the Arctic Ocean but speculated that meddies could be generated by the same mechanism as the Mediterranean outflow separates from the continental slope. In fact, [Bower et al. \(1997\)](#) conclude from the interpretation of a number of Lagrangian observations that the conceptual model of D'Asaro accounts for the preferred spawning of meddies at Cape St. Vincent. [Prater \(1992\)](#), however, could not find evidence that the Gulf of Cadiz meddy was a result of vorticity generation in a viscous shear layer. He concluded that the most likely generation mechanism for the Gulf of Cadiz meddy is the instability of a coastally bounded jet, and he compared his findings with laboratory experiments for a buoyant surface current ([Griffiths and Linden 1981](#)). In the laboratory experiments the instabilities manifested themselves in a wavelike manner. The crests consisted of anticyclonic vorticity and were rich in source water, whereas the troughs showed cyclonic motion and low source water content. The problem of an intermediate depth boundary current within a stratified environment was studied experimentally by [Baey et al. \(1995\)](#) using a 13-m diameter rotating tank. In a three-layer configuration, the intermediate water layer, which initially was prescribed to flow geostrophically along the (vertical) wall of the tank, became unstable for a certain range of parameter settings. For small Burger and Ekman numbers, [Baey et al. \(1995\)](#) observed the generation of dipoles that were shed into the interior. In some cases, isolated anticyclonic lenses were generated, resembling meddies. The result stressed by the authors to be most important is that isolated lenses may be generated in the absence of any topographic effects. [Käse et al. \(1989\)](#) modeled a meridional jet, representing the Mediterranean outflow as it moves north after passing Cape St. Vincent. The instabilities produced cyclonic and anticyclonic eddies, but the cyclones were shed to the east and therefore bound between the jet and the coastline. The numerical simulations were carried out with a quasigeostrophic model and did not account for the boundary current character of the Mediterranean outflow. The stability of a bottom-trapped coupled density front (a vein of dense water) was investigated by [Griffiths et al. \(1982\)](#), [Swaters \(1991\)](#), and [Jiang and Garwood \(1996\)](#). [Swaters \(1991\)](#) presented a theoretical model and a linear stability analysis for a dense bottom vein on a sloping continental shelf. His two-layer model takes into account nonquasigeostrophic effects (i.e., perturbations in the plume height are not small in comparison with the height of the front itself). The instability is baroclinic in the sense that mean potential energy is released by the downslope slumping of the perturbed density front on the downslope edge of the dense filament. The density front is strongly coupled to the upper layer through the mechanism of vortex stretching and compression. The perturbations are manifested in the form of amplifying anticyclones on the downslope density front. In the ambient slope water they appear as growing topographic Rossby waves. In an experimental setting resembling the Denmark Strait overflow, [Jiang and Garwood \(1996\)](#) used a three-dimensional numerical model and showed that the bottom plume becomes unstable and smaller subplumes break off from the mean bottom flow and travel downslope, thus accounting for a considerable amount of cross-isobath transport. As in [Swaters's \(1991\)](#) model, the lower-layer flow (the density current) is strongly coupled to the upper layer. Eddies are formed in the upper layer and travel in a direction with the shallower water to their right. Similar vortices, resembling topographic Rossby waves, were also found in the experiments of Jungclaus and Mellor (1999, JM hereafter). In

our previous study, however, we did not consider downslope slumping subplumes, but warm and saline anomalies were periodically injected laterally at a depth range between 1000 and 1500 m. We concluded that a similar mechanism as described by [Swaters \(1991\)](#) and [Jiang and Garwood \(1996\)](#) was the cause of this instability. The complicated bottom topography (which was chosen to realistically simulate the pathway and the water mass transformation within the Mediterranean outflow), however, did not allow us to discriminate between hydrodynamic instabilities and topographical effects such as canyons and the sharp bend of the coastline at Cape St. Vincent that were previously considered as generation mechanism for meddies. In the study presented here, we therefore wish to go back to a more simplified model setting to study the evolution of a density current within a stratified environment separately from the effect of topographic variations. The main difference between this study and the one by [Jiang and Garwood \(1996\)](#) is that here the dense water flows into a strongly stratified environment where the initial density contrast is quickly eroded so that the plume finds its equilibrium density at an intermediate depth level.

The paper is organized as follows. In [section 2](#) the numerical model and the model setup is described. The standard experiment, discussed in [section 3](#), uses mean parameters taken from the Mediterranean outflow west of Gibraltar. Additional sensitivity studies are included ([section 4](#)) to investigate the effect of topographic disturbances such as canyons and ridges. We conclude with a summary and discussion.

## 2. The numerical model

The model used here is the three-dimensional, sigma-coordinate Princeton Ocean Model of [Blumberg and Mellor \(1987\)](#). The terrain-following vertical coordinate with enhanced resolution in the bottom boundary layer was successfully applied to the Mediterranean outflow in the Gulf of Cadiz by JM. The model demonstrated the routing of the flow by canyons in the Gulf of Cadiz, and the water mass transition in the outflow layer agreed favorably well with observations. Particularly, the simulated vertical shape of the horizontal velocity profile within the dense bottom current was in good agreement with the observations of [Johnson et al. \(1994\)](#). The primitive equation model utilizes the hydrostatic and Boussinesq approximations and has a free surface. Since Rossby numbers  $Ro > 0.1$  are to be expected, nonlinear effects will be important. However, even for vigorous downslope movement during the adjustment phase, the product of Rossby number and aspect ratio (i.e., the height of the outflow plume divided by its width) is  $\ll 1$ , and therefore nonhydrostatic effects can be neglected ([Jiang and Garwood 1996](#)). Vertical turbulent mixing processes are parameterized with the second-order turbulence closure scheme of [Mellor and Yamada \(1982\)](#). At the surface there is no wind stress and there are no heat and salt fluxes. At the bottom the drag coefficient is determined by matching the velocity profile to the logarithmic law of the wall

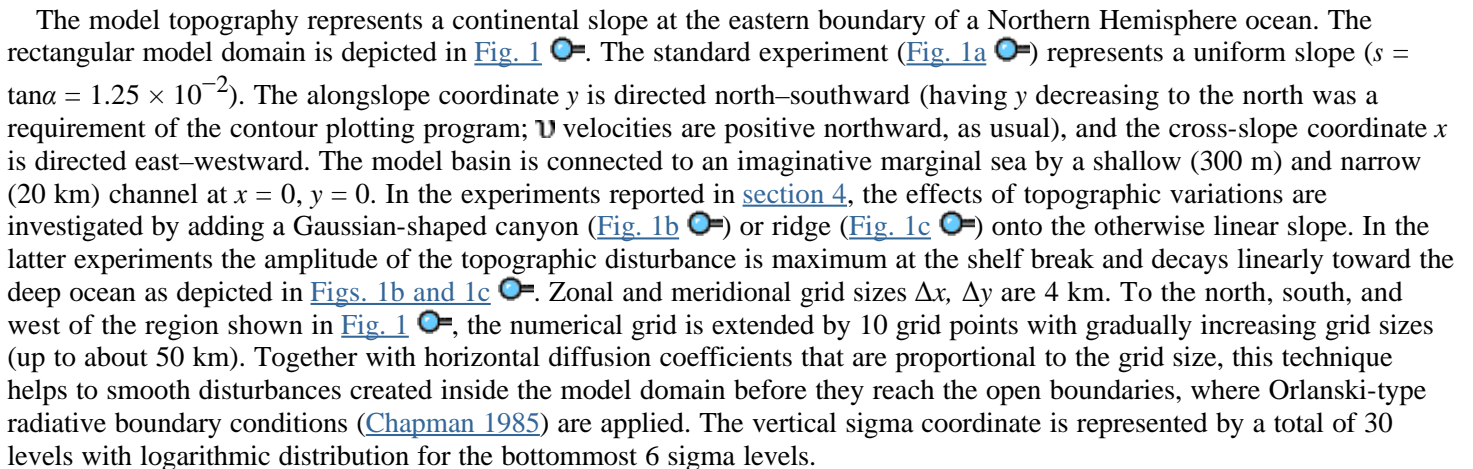
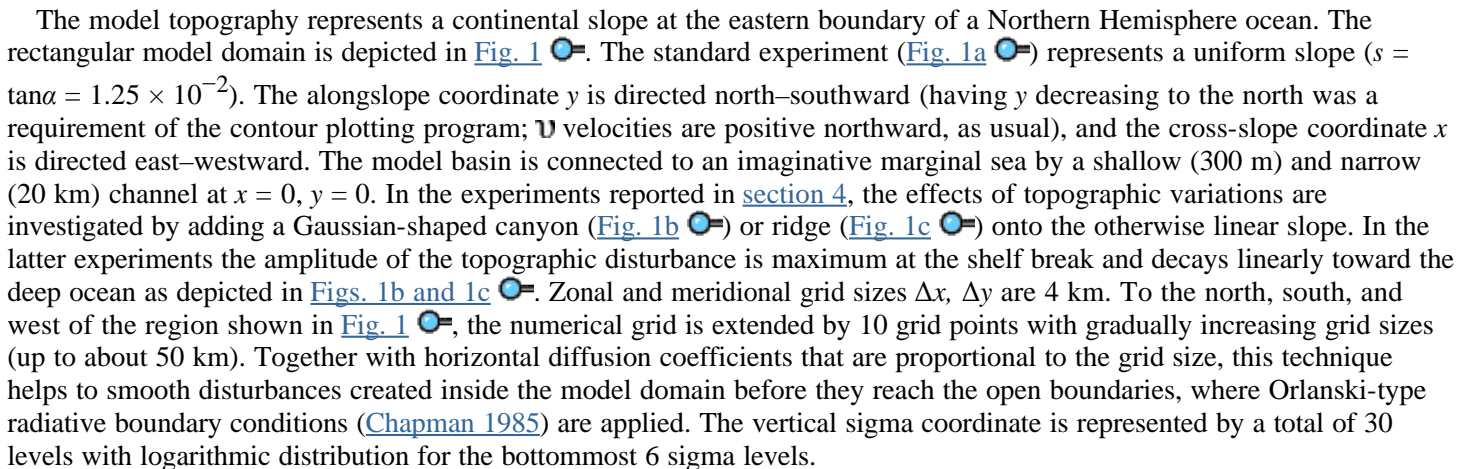
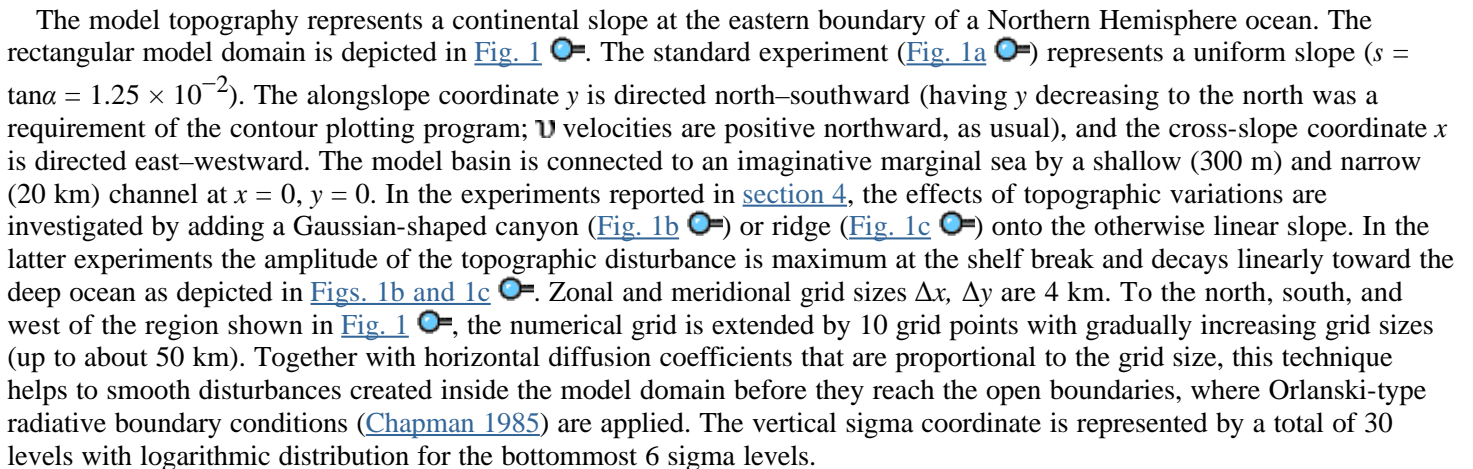
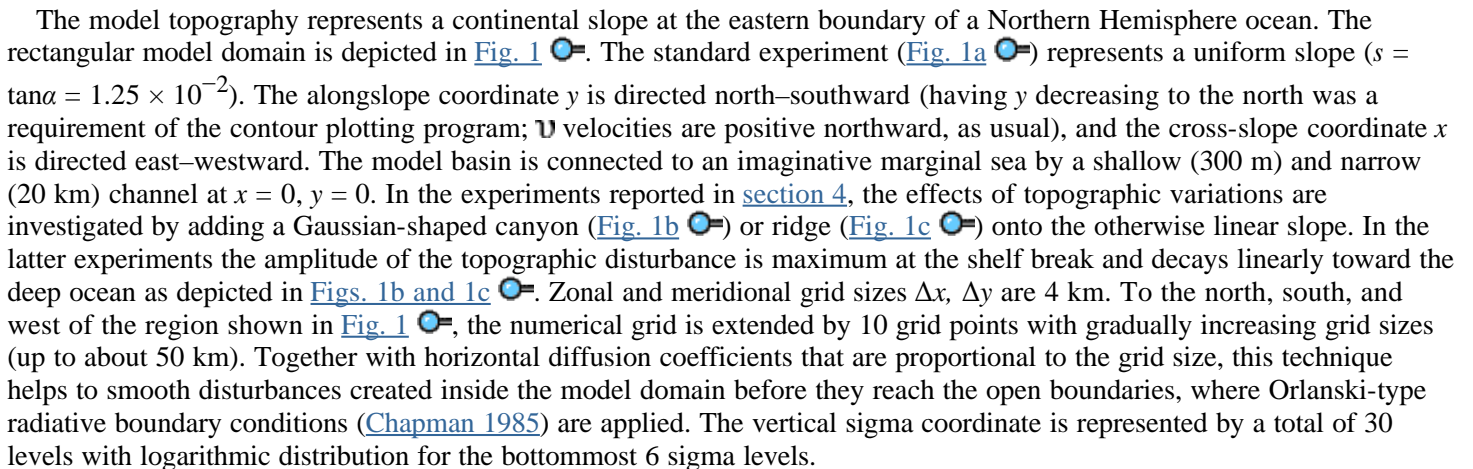
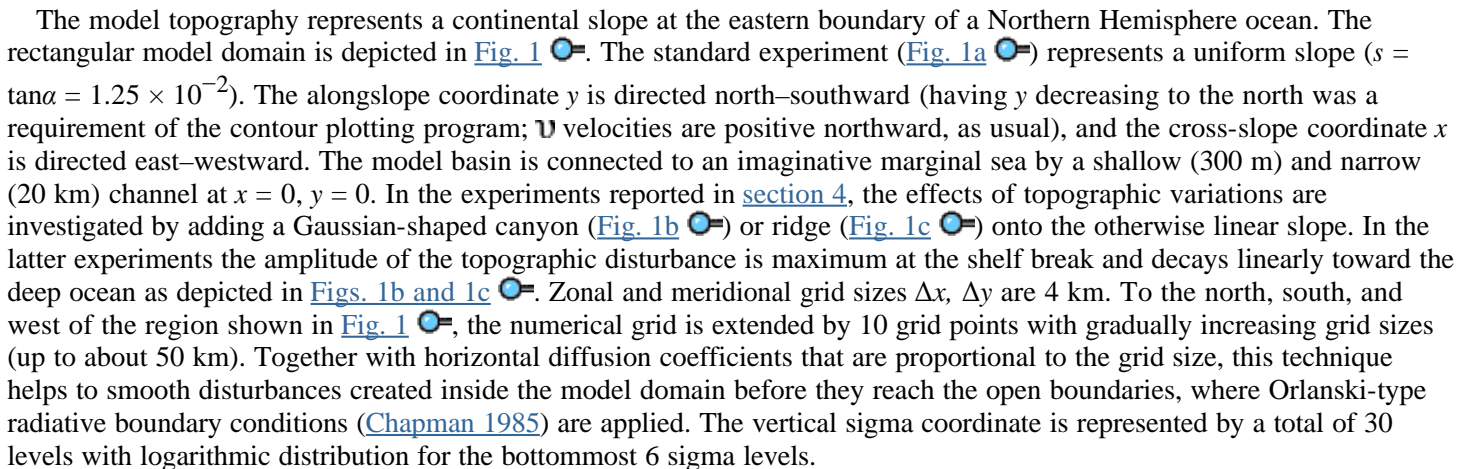
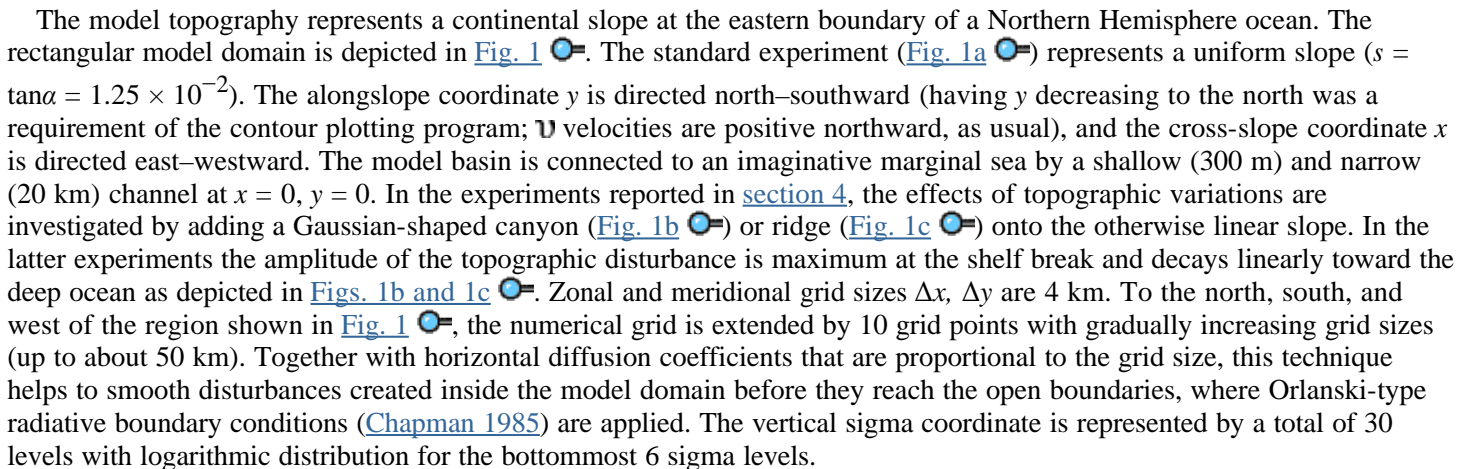
$$c_D = \max[2.5 \times 10^{-3}, \kappa^2 \ln(\Delta z_b/z_0)^{-2}],$$

where  $\kappa$  is the von Kármán constant,  $z_0$  is the roughness length (1 cm), and  $\Delta z_b$  is the distance of the deepest velocity grid point from the bottom. Laplacian friction is implemented along sigma surfaces using the formulation of [Smagorinsky \(1963\)](#)

$$A_M = A_H = C\Delta x\Delta y[u_x^2 + \mathbf{v}_y^2 + (u_y + \mathbf{v}_x)^2/2]^{1/2},$$

where a value,  $C$ , of 0.05 is applied. Mean  $T(z)$  and  $S(z)$  profiles are subtracted prior to the calculation of the diffusion to minimize artificial cross-isopycnal diffusion ([Mellor and Blumberg 1985](#)). For further information on the POM model, the reader is referred to earlier publications (e.g., [Blumberg and Mellor 1987](#)).

### a. Model domain, lateral boundary conditions, and initial conditions

The model topography represents a continental slope at the eastern boundary of a Northern Hemisphere ocean. The rectangular model domain is depicted in [Fig. 1](#) . The standard experiment ([Fig. 1a](#) ) represents a uniform slope ( $s = \tan\alpha = 1.25 \times 10^{-2}$ ). The alongslope coordinate  $y$  is directed north–southward (having  $y$  decreasing to the north was a requirement of the contour plotting program;  $\mathbf{v}$  velocities are positive northward, as usual), and the cross-slope coordinate  $x$  is directed east–westward. The model basin is connected to an imaginative marginal sea by a shallow (300 m) and narrow (20 km) channel at  $x = 0, y = 0$ . In the experiments reported in [section 4](#), the effects of topographic variations are investigated by adding a Gaussian-shaped canyon ([Fig. 1b](#) ) or ridge ([Fig. 1c](#) ) onto the otherwise linear slope. In the latter experiments the amplitude of the topographic disturbance is maximum at the shelf break and decays linearly toward the deep ocean as depicted in [Figs. 1b and 1c](#) . Zonal and meridional grid sizes  $\Delta x, \Delta y$  are 4 km. To the north, south, and west of the region shown in [Fig. 1](#) , the numerical grid is extended by 10 grid points with gradually increasing grid sizes (up to about 50 km). Together with horizontal diffusion coefficients that are proportional to the grid size, this technique helps to smooth disturbances created inside the model domain before they reach the open boundaries, where Orlanski-type radiative boundary conditions ([Chapman 1985](#)) are applied. The vertical sigma coordinate is represented by a total of 30 levels with logarithmic distribution for the bottommost 6 sigma levels.

At the inflow–outflow channel, profiles of temperature, salinity, and velocity are prescribed (Fig. 2a), taking into account observed values from the western approaches of the Gibraltar Strait (Kinder and Bryden 1990). The flow is assumed to be uniform over the width of the narrow inflow–outflow channel. There is a bottom-intensified saline inflow and an outflow of less saline AW within the upper 200 m. The inflow and outflow transports of 0.8 Sv ( $1 \text{ Sv} = 1 \times 10^6 \text{ m}^3 \text{ s}^{-1}$ ) are assumed to be equal so that the model does not gain or lose mass. The ambient stratification (Fig. 2b) was constructed using typical profiles from the Gulf of Cadiz, not directly influenced by the Mediterranean outflow (Baringer 1993). However, as can be seen clearly from the salinity profile, there is a maximum at about 1200 m originating from the long-term diffusion of MW into the Atlantic at this particular depth. Note that there is a relative minimum in stratification and static stability in the depth level influenced by the Mediterranean water. The model uses a  $\beta$ -plane approximation with  $\beta = 1.98 \times 10^{-11} \text{ (m s)}^{-1}$  and  $f_o = 7.75 \times 10^{-5} \text{ s}^{-1}$  (centered around  $36^\circ\text{N}$ ).

### 3. The standard experiment

#### a. Characteristic features of the unstable boundary current

The experiment is started from rest and the prescribed normal velocities are slowly (within one inertial period) raised to their steady value and kept constant during the rest of the experiment, which lasted for more than three years (1120 days). The model was started from a point where no Mediterranean outflow water was present in order to have the model find a quasi-steady state on its own. In this study we are not interested in the initial evolution of the boundary current and therefore describe the general model results after a time long enough for the head of the gravity current and associated transients to leave the open boundary of the model domain. Figure 3a shows the near bottom ( $\sigma$ -level 28) salinity field after 320 days of integration. The fronts of the saline outflow current are indicated by the 36.3-psu isohaline. Near the source at  $x = 0, y = 0$  the plume moves downslope in a balance between the downslope pressure gradient and bottom friction as described by Jungclaus and Backhaus (1994). As the plume accelerates, it is deflected to the right into a direction parallel to the depth contours by the Coriolis acceleration. Turbulence, mainly created by the strong shear between the MW layer and the ambient, leads to the entrainment of considerable amounts of ambient water into the plume. The excess density contrast quickly decreases as is visible by the erosion of the core bottom salinity from 38 psu at the source to 37.3 psu within the first 30 km of its pathway. Downstream of  $y = -100 \text{ km}$ , the flow merely follows isobaths and the salinity decreases only moderately thereafter. The highest salinities at the northern end of the model domain exceed 36.6 psu. The downslope edge of the plume follows the 1700-m depth contour for more than 400 km, and there is no indication of a further downslope spreading of the outflow by Ekman veering. A space–time plot of the near bottom salinity, taken at  $y = -320 \text{ km}$ , is depicted in Fig. 3b. Although there is some upslope excursion of the downslope front at the end of the second and third model year, the core of the saline tongue almost remains at a fixed depth level. It is interesting to compare the bottom salinity field with a respective figure from the study of Jiang and Garwood (1996, e.g., their Figs. 7, 8). In a similar experimental setting, but using a lower initial density contrast and a homogeneous ambient, they found large excursions of the lower edge of the boundary current that developed into downslope slumping subplumes. These subplumes or domes of detached dense water are absent in the experiment described here over the entire runtime. However, a control run with constant temperature and salinity in the ambient slope water (not shown here) gave similar results as reported by Jiang and Garwood (1996). The bottom subplumes and surface eddies were somewhat larger in the control experiments, owing to the larger initial density difference.

A closer inspection of the three-dimensional temperature and salinity field of the standard run reveals that the outflow current, which is initially aligned to the topography, meanders periodically and eventually forms lateral injections of warm saline water at middepth. We conclude that the ambient stratification prevents the downslope movement of developing disturbances of the bottom boundary current. Instead they penetrate into the ambient water at their respective density horizon and undergo an adjustment process.

To demonstrate the continuous formation of lenses that carry outflow water offshore, Fig. 4a shows a space–time plot of the 1150-m salinity taken at  $y = -350 \text{ km}$ . Shedding events occur approximately every 100 days, are of different intensity, and possess often double maxima. The disturbances show a pronounced westward (offshore) propagation with a phase speed of  $2\text{--}4 \text{ cm s}^{-1}$ . In Fig. 4b a limited section of the same figure is depicted together with a space–time plot of relative vorticity in Fig. 4c. The relatively broad patch of saline water that leaves the western boundary around day 340 is accompanied by anticyclonic circulation. This indicates that the westward transport is accomplished by an anticyclonic eddy. Tracing the negative vorticity streak back to day 325, one finds a broad cyclonic region that is apparently moving in a more northward direction. On the other hand, the high salinity flow out of the model domain around day 310 is associated with elongated streaks of both anticyclonic and cyclonic vorticity. This indicates a dipole moving westward. It is clear from the slope of the vorticity streaks that the dipole possesses a considerably higher phase velocity than the following anticyclonic monopole. The propagation characteristics of the dipoles and isolated anticyclones will be discussed in more detail in section 3c. In the wake of cyclonic circulation regions (e.g., day 320, day 360) there is an inflow of water with ambient water mass characteristic into the model domain driving the salinities back below 36.3 psu.

A typical horizontal view upon the middepth salinity field is given in [Fig. 5](#). It shows the salinity at the 1150-m depth level after 320 days of integration. Upstream of  $y = -175$  km, the outflow is visible as a narrow boundary current aligned to the topography. Farther downstream a tongue of saline water has formed that extends over the width of the model domain. Centered at  $y = -410$  km and  $x = -200$  km there is a strong anticyclonic eddy with a core salinity exceeding 36.6 psu. At this stage of development the eddy is still attached to the outflow and saline water is advected from the east into the lens. Ahead of the eddy, the anticyclonic motion advects ambient water and enhances the salinity gradient, leading later to a detachment of the lens. Salinities higher than 36.3 psu are also visible at the northern boundary, and this is the wake of an earlier shedding event. At  $y = -190$  km,  $x = -80$  km, close to the continental slope, the velocity vectors show a meander and one observes an offshore excursion of the high salinity outflow water. As we will discuss later in more detail, this is the initial stage of another large-amplitude shedding event.

[Figure 6a](#) shows the sea surface elevation together with the velocity vectors at 20-m depth. In the wake of the middepth salinity tongue (upstream of  $y = -400$  km) there is a broad region of negative sea surface anomalies, indicating cyclonic circulation, followed by positive surface heights near  $y = 0$ . These relatively broad features travel to the north in the direction having the shallower water to their right and resemble topographic Rossby waves. While the velocity vectors suggest that the flow is generally not barotropic, there is anticyclonic circulation directly above the saline lens at middepth, corroborating the findings of [Käse et al. \(1989\)](#) and [Stammer et al. \(1991\)](#) that meddies can have a pronounced surface expression. These signatures in surface heights and speeds are also visible in the space–time plot of near-surface relative vorticity in [Fig. 6b](#) where the anticyclonic feature displayed in [Fig. 4c](#) is detected. The relatively broad cyclonic features that occur predominantly in the wake of the lateral intrusions show a less elongated form and travel apparently to the north in the direction of the bottom boundary current.

The overview of the three-dimensional flow structure at  $t = 320$  days is completed by an inspection of vertical sections in [Fig. 7](#). [Figures 7a–d](#) show sections through the boundary current at  $y = -100$  km, rather close to the source but where the maximum velocities are directed predominantly along the slope. The salinity and velocity sections show the bottom boundary current as a thin (about 150 m) and fast moving (maximum velocities exceeding  $0.4 \text{ m s}^{-1}$ ) layer of dense water underlying a rather quiescent upper water body. The isohalines and isopycnals reverse slope close to the topography indicating a well mixed layer with a thickness of about 10–50 m. This shape of the isopycnals is typical for a situation where an alongslope current favors a downslope Ekman flux in the presence of stratification ([Weatherly and Martin 1978](#)). Relatively light water is advected under denser water, leading to static instability and enhanced vertical mixing. The reversal of the isopycnal slope near the bottom has also a dynamical consequence. According to [MacCready and Rhines \(1993\)](#), the associated baroclinic pressure gradients tend to decelerate the alongslope flow near the bottom more efficiently than bottom friction. Eventually any cross-slope Ekman flux is shut down. This effect occurs, however, most pronounced at the upslope edge of the boundary current where light ambient water is transported downslope under the outflow. The mixed layer depth decreases downslope and there is a near-bottom density maximum of  $\sigma_\theta > 28.2 \text{ kg m}^{-3}$  at 1500 m. Below this depth, downwelling of relatively dense water occurs, and shut down is not expected there as was demonstrated by [Ezer and Weatherly \(1990\)](#). Note that the downslope Ekman transport has transported the saltiest water into the lowest part of the vein. On the other hand, the density contrast between the outflow and the ambient water decreases rapidly downslope owing to the ambient stratification. In fact, the baroclinic pressure gradients driving the outflow vanish below 1750 m. This inhibits effectively any further downslope spreading. At middepth the density contrast between the bottom boundary current and the ambient slope water reads about  $0.35 \text{ kg m}^{-3}$  so that we arrive at an internal Rossby radius of roughly 10 km.

[Prater \(1992\)](#) has shown that one defining characteristic of meddies is their low potential vorticity (PV) and that this PV anomaly can be traced back to the Mediterranean Undercurrent. [Figure 7b](#) depicts the regions of the flow where the potential vorticity is reduced compared to the mean PV field in the absence of the outflow (the in situ PV is normalized by the background PV at matching depth). Within the outflow layer the PV is smaller by more than one order of magnitude. [Figures 7e–h](#) demonstrate how the character of the outflow changes downstream. This section is taken at  $y = -395$  km, cutting through the developing anticyclonic lens. Near the continental slope, the outflow is deflected offshore and has lost its character as a bottom boundary current. Water influenced by the outflow, characterized by high salinity and low PV, extends laterally far into the interior. Isopycnals are uplifted above 1000 m and show a lenslike deformation from their initial state ([Fig. 7g](#)). The salinity of the interior ([Fig. 7e](#)) has increased over a depth range from 500 to 1750 m. Although the highest salinities are found between 1200 and 1500 m, the anomalies owing to the advection of outflow water into the ambient are visibly most pronounced in the depth range above 1100 m. This is seen clearly in the PV anomaly field ([Fig. 7f](#)), where, for clarity, only regions with reduced PV are depicted. The PV is reduced by a factor of 10 compared to its background value within the anticyclonic eddy. There is also a secondary maximum below 1500 m. Here some of the saltiest water that was visible on the continental slope in [Fig. 7a](#) intruded into the ambient and increased the isopycnal separation between the  $\sigma_\theta = 28.0$  and  $28.1 \text{ kg m}^{-3}$  isopycnals. The velocity field indicates an anticyclonic eddy centered at  $y = -200$  km and 850-m depth. Although there are pronounced velocity maxima at middepth, there is no change of sign in the water column above and beneath the core of the eddy, corroborating the earlier finding that there is a considerable barotropic velocity component. The core radius taken from the distance of the velocity extrema reads 27 km. This is consistent with the size of observed saline lenses in the Canary and Iberian Basins ([Armi and Zenk 1984](#); [Käse and Zenk 1987](#)) Other

meddies, such as the Gulf of Cadiz meddy described by [Prater and Sanford \(1994\)](#) with its core radius of 9 km, were considerably smaller. The meddy described by [Schultz Tokos and Rossby \(1991\)](#) possessed the maximum PV anomaly at a depth of 1200 m, and [Prater and Sanford \(1994\)](#) report a double core structure with PV minima at 1050 and 1400 m. The depth of the velocity maxima of observed meddies varies also considerably. While [Prater and Sanford \(1994\)](#) show a maximum of azimuthal velocity at 1050 m, the meddy that was observed by [Siedler et al. \(1985\)](#) in the Canary Basin had the highest velocities at about 800 m. Apparently, the properties found within the meddies reflect those of the different formation sites. The Gulf of Cadiz meddy ([Prater and Sanford 1994](#)), for example, owes its double core structure to the two branches of the Mediterranean Undercurrent that are separated by a few hundreds of meters vertically on the continental slope south of Portugal. In the Gulf of Cadiz, the outflow current is strongly routed by the topography ([Zenk 1975](#)), and we simulated the separation in our experiments with realistic topography (JM). Here, using a uniform slope topography, this effect is absent and the velocity maximum of the boundary current stays at a shallower depth. Of course, also the strongest meandering and eddy shedding are then expected to occur at this depth level. In addition, in a flow that is routed more strongly by the topography, we expect the velocity and salinity maxima to be aligned more closely.

In [Figs. 7b,f](#) we have shown that the bottom boundary current near the continental slope and the anticyclonic eddy are regions of low potential vorticity. Potential vorticity was calculated using Eq. (A1) given in the appendix. The mean (background) PV is modified by contributions from the in situ relative vorticity, stratification, and vertical shear terms. To understand how the low PV is introduced and how it is maintained in apparently different flow regimes, we show vertical profiles of the three components relative vorticity (given by the Rossby number  $Ro$ ), buoyancy anomaly  $G$ , and the vertical shear (given by the Froude number  $F$ ). Within the thin outflow layer ([Fig. 8a](#)) the Froude number possesses two maxima, one above and one below the velocity maximum, indicating the shear regions near the bottom and in the transition region to the overlaying waters. The Froude number term is always positive but appears in Eq. (A1) with a negative sign thus contributing to a considerable reduction of PV. In the well-mixed bottom boundary layer the stratification term reaches its minimum value  $-1$  but exceeds 1 in the strongly stratified transition region between the outflow and the ambient waters. The relative vorticity changes sign in the bottom and interfacial shear layers but contributes relatively little to the total PV. Farther upstream the Froude number term is even more dominant and  $F$  exceeds 4 (indicating a Richardson number  $<0.25$ ), where intense vertical mixing occurs. We conclude that the low PV is initially created by the vertical shear of the horizontal velocities, which owes its existence to frictional stresses at the bottom and at the interface. Subsequently, there is enhanced turbulent mixing in the shear layers and entrainment of ambient water increases the thickness of the bottom boundary current (and finally reduces the vertical shear). [Figure 8b](#) shows a profile from a location 240 km downstream (at the same bottom depth), where the core of the saline tongue is deflected offshore. Westward flow has advected outflow water into the interior causing the isopycnals bounding the outflow, which were seen to slope strongly upward above the bottom boundary current in [Figure 7c](#) to flatten. The thermal wind relation then requires a reduction of vertical shear reducing the Froude number term significantly. Compared to the background, however, the intruding plume has a lower stratification so that low PV is maintained within the tongue by the  $G$  term. As the outflow penetrates into the ambient water, it deforms the (initially horizontal) isopycnals. The horizontal density gradients reintroduce vertical shear by thermal wind constraints. The lens-shaped disturbance requires a velocity extrema in the (vertical) center of the lens. Here the disturbance is a high pressure center and supports anticyclonic circulation. The adjustment goes along with a transfer of eddy potential energy into eddy kinetic energy. Thus, during the development of a meddy, negative vorticity is introduced in expense of the buoyancy term. This can be seen in [Fig. 8c](#), a profile directly from the center of the anticyclone displayed in [Fig. 7f](#). The buoyancy anomaly term shows a minimum of  $-0.8$ , and the relative vorticity term reads  $-0.35$  [note that the nonlinear term in (A1) gives a positive contribution adding the PV anomaly factor to  $-0.87$  at 850-m depth]. The  $G$  term is positive below 1150 m and above 700 m. Here the ambient stratification has increased as a result of the intrusion, and the upper and lower part of the water column are compressed. Anticyclonic circulation is required to conserve potential vorticity. The relative vorticity therefore is negative throughout the water column, and the azimuthal velocity of the meddy possesses a barotropic component of a few centimeters per second. We have seen the surface expression in [Fig. 6a](#), but a closer inspection of the bottom velocity field ([Fig. 3a](#)) reveals anticyclonic circulation also underneath the meddy. It is an observed feature that meddies possess a pronounced surface signature (e.g., [Käse and Zenk 1987](#)), and imprints of meddies in the depth range 200–3000 m have been reported from a moored current meter array in the Canary Basin ([Siedler et al. 1985](#); [Käse and Zenk 1996](#)).

### *b. Indication for baroclinic instability*

[Jiang and Garwood \(1996\)](#) concluded that the most likely generation mechanism for the breaking off of their dense bottom current was the baroclinic instability theory of [Swaters \(1991\)](#). Swaters used a two-layer configuration and investigated the linear instability of a bottom-trapped coupled front. He explicitly excluded any barotropic instability processes associated with horizontal shear of the mean current. In our numerical study, the evolution of large amplitude meanders is essentially nonlinear, and, in addition, we cannot rule out that horizontal shear contributes to the destabilization. However, it is interesting to describe qualitative similarities between the destabilization of [Swaters's \(1991\)](#) cold vein and the perturbations found here. Swaters's theory takes into account that the dynamics of the coupled front (the density current), while geostrophic, is not quasigeostrophic because frontal height deflections are of the same order as the frontal height scale. Swaters showed that the instability is driven by the release of mean potential energy by the downslope slumping subplumes. Swaters notes that “if baroclinic instability occurs, then, on average, the correlation between the cross-shelf




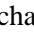
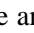
flow and frontal height anomaly must be positive.” Positive frontal height anomaly refers to a positive density anomaly, and an offshore flux of relatively dense water is required, which we clearly see in our experiments. As has been pointed out by [Karsten et al. \(1995\)](#), the associated onshore flow (towards shallower water) of relatively light ambient water can be seen as equivalent to the northward flux of heat required in midlatitude baroclinic instability in the atmosphere. In terms of potential vorticity, a necessary condition for baroclinic instability to occur ([Swaters 1991](#)) is that PV must increase offshore within the bottom boundary current. [Figure 7b](#) shows that the core of the density current is a minimum of PV so this quantity increases both onshore and offshore. Thus, this condition is met within the density current.


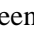
To understand how the large meanders, dipoles, and isolated lens form it is necessary to focus the attention on the early stage of their development. In [Fig. 5](#) we saw that the outflow begins to meander about 100 km downstream of the source. [Figure 9](#) depicts a meridional section (parallel to the coast) taken at  $x = -70$  km at the same instant of time. The cross-shore (perturbation) velocity component is shown in [Fig. 9a](#). There is offshore (negative) motion and onshore motion and the highest velocities are found at a depth between 800 and 1000 m, where also the alongslope speeds were highest. The most notable feature is that the shear of the perturbation velocity leans against the mean shear. The density field demonstrates the interaction between the intruding outflow water and the ambient water. For example, the offshore flow centered at  $y = -190$  km pulls dense water away from the outflow and leads to an uplifting of the isopycnals. The vertical axis of most pronounced uplifting shows a similar tilt as the velocity shear ([Fig. 9a](#)). Thus, the upper-layer pressure wave leads the lower layer (the perturbed density current) in the same manner as in the study of [Swaters \(1991\)](#). This phase relationship is necessary for the release of potential energy from the mean flow into the perturbations and indicative of baroclinic instability (e.g., [Gill 1982; Swaters 1991](#)). Upstream of the intrusion the isopycnals show a depression. This can be seen for the  $\sigma_\theta = 27.35$  isopycnal at  $y = -247$  km and  $y = -175$  km. Here the upper water column is stretched and cyclonic vorticity is introduced leading to the surface flow pattern seen in [Fig. 6](#).

### *c. Lens formation and meddy propagation*

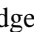
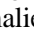


In the following, the formation of one single meddy is described in detail by displaying a sequence of salinity and velocity snapshots from the 1150-m-depth level in [Fig. 10](#). Although we have seen that the highest anomaly in PV occurs above 1000 m, we prefer to visualize the traditionally defining property of a meddy, the enhanced salinity at middepth. The meddy formation documented in [Fig. 10](#) appeared after approximately 60 days of integration, rather early in the simulation, but it was chosen because the ambient water was least contaminated by earlier shedding events at this stage, and the details of the detachments are most clearly seen here. At  $t = 64$  days ([Fig. 10a](#)) the outflow current starts to deviate from the alongshore direction approximately at  $y = -380$  km. The velocity vectors bend back to the north somewhat downstream so that inside the saline layer there is a meander with anticyclonic vorticity, while farther upstream cyclonic vorticity dominates. This is the early state of the formation of a dipole. Twelve days later ([Fig. 10b](#)) this dipolar structure can be seen more clearly. The anticyclone is intensifying as it is filled by saline outflow water from the east. The influx of relatively dense water increases the lateral baroclinic pressure gradients and leads to enhanced vertical shear by thermal wind constraints. In contrast, on the upstream side of the cyclone, water of ambient characteristic is advected shoreward. Relatively fresh water is transported into the cyclonic region from the southwest. This northwestward flow also pushes the salinity front northward (at  $x = -100$  km,  $y = -400$  km) and results in a narrowing of the saline tongue. This supports the pinching off of an isolated saline region. Another six days later the anticyclone has moved 30 km to the west but only slightly northward, it no longer travels with the generally northward moving plume at the boundary. Since the cyclone continues its northward propagation the axis connecting the vortex centers is tilted in a more and more zonal orientation so that the anticyclone circumvents the cyclonic region in an anticlockwise sense. While the anticyclone possesses a detached salinity maximum of  $S > 36.6$  psu, ambient water is carried into the tail of the tongue both by the cyclonic circulation on its southern side and by the anticyclonic circulation in the north ( $y = -420$ ,  $x = -150$  km). Finally, the lens detaches completely from the outflow current and starts to move into a southward direction. At  $t = 172$  days it is visible about 90 km away from its separation location as an isolated saline lens. A newly formed meander is visible north of  $y = -450$  km and at  $x = -100$  km,  $y = -340$  km, offshore deflection of the outflow water in the boundary current indicates the initial phase of another shedding event. In the meddy, the core salinity has reduced to about 36.4 psu and also the azimuthal velocities have decreased from 13 to less than  $10 \text{ cm s}^{-1}$ . This decay is relatively fast compared with observations where, for example, azimuthal velocities of about  $20 \text{ cm s}^{-1}$  were still observed some hundreds of days after the estimated formation ([Schultz Tokos and Rossby 1991](#)). Numerical diffusion (introduced mainly to keep the central-difference advection scheme from producing over and undershoots) is probably too high, and the numerical resolution of the order of the internal Rossby radius is still too coarse to adequately resolve smaller-scale processes. It would be probably advantageous to introduce a more scale selective biharmonic diffusion. The horizontal diffusion of plume anomalies in this model is directed along sigma surfaces that may introduce some artificial diapycnal diffusion. However, the diffusion along sigma surfaces were retained because experiments by [Mellor and Blumberg \(1985\)](#) indicate that a diffusion operator, which rotates diffusion to horizontal planes, did not maintain a valid bottom boundary layer behavior, which is crucial for the simulation of the dense bottom flow. Another reason for the relatively weak anomalies may be related to the fact that in the present model setting, the ambient stratification is assumed to be horizontally uniform, whereas in reality the ambient salinity maximum at middepth decays with distance from the slope. A meddy traveling into less saline and colder water would show a larger anomaly in salinity and temperature [[Armi and Zenk \(1984\)](#) found, e.g., a meddy with a core salinity of 36.4 psu within a layer of 35.6 psu water in

The meddy generation scenario presented here bears striking resemblance to the laboratory experiments of [Baey et al. \(1995\)](#). They describe the formation of an anticyclonic meander at the offshore side of the boundary current that intensifies and finally develops into a dipole that is shed from the boundary. Depending on the parameter setting, either the dipole detached from the boundary current or only the anticyclonic part of it survived. Also in their experiment there were cyclonic vortices visible in the upper layer. The size of the lenses was two times the Rossby radius, whereas the eddies simulated here are about five times the Rossby radius. According to [Gill \(1981\)](#), the aspect ratio of a homogeneous intrusion into a stratified fluid depends on the ambient stratification so that differences between a laboratory three-layer setting and the continuous stratification applied here are to be expected.

Summarizing the meddy detachment process, the pathways of selected vortices are depicted in [Fig. 11](#) . The meddy described above together with the cyclonic eddy that was initially associated to it is indicated in [Fig. 11a](#) . The initially westward movement with a small northward component owing to the attachment to the boundary current is stopped when the lens separates completely. The lens shows an anticlockwise movement circumventing the cyclonic region to the east of it. Between day 88 and 172 it moves predominantly southward, but there is a slight eastward component visible. The propagation velocity is considerably smaller ( $1.3 \text{ cm s}^{-1}$ ) than during the initial westward movement ( $4 \text{ cm s}^{-1}$ ). The following event (indicated by the squares in [Fig. 11a](#) ) differed considerably from the first. Here the dipole that initially departed from the outflow current did not break up into counterrotating eddies but moved in a predominantly westward direction carrying water with a high concentration of outflow water in the center. Another event that resulted in an isolated anticyclonic lens is documented in [Fig. 11b](#) . Although the lateral excursions are larger the translation characteristics resemble the first meddy shown in [Fig. 11a](#) . Also here the dipolar structure breaks off and the cyclone and anticyclone develop meridional translation components of opposite sign. Unfortunately we were not able to track one eddy for more than, say 100–150 days. Either they were caught by the following meanders or left the western model domain. A common feature of the simulated vortices is that zonal (westward) motion was dominant in the initial phase that is characterized by a dipolar circulation structure. While dipoles tend to move into a direction perpendicular to the axis connecting their centers ([Käse and Zenk 1996](#)), isolated eddies possess meridional translation components in an ocean with an ambient vorticity gradient ([McWilliams and Gent 1986](#)). The southwestward motion of an anticyclone has been simulated, for example, by [Beckmann and Käse \(1989\)](#). An initially circular vortex loses vorticity by emitting Rossby waves. The asymmetry of this process deforms the core elliptically, and a meridional translation is introduced in the direction of the respective ambient vorticity gradient. The propagation speed of the simulated meddy was  $0.8 \text{ cm s}^{-1}$ . The translation of observed meddies is, however, in part influenced by the large-scale velocity field characterized by subtropical recirculation. [Shapiro et al. \(1995\)](#) estimate that the self-propelling motion due to the  $\beta$  effect accounts for a few millimeters per second of the  $1\text{--}4 \text{ cm s}^{-1}$  propagation speed of observed meddies.

The pathways indicated in [Fig. 11](#)  are, however, consistent with the observed float trajectories reported by [Käse and Zenk \(1996\)](#). The meddies (depicted in their Figs. 12.7, 12.8, and 12.9) were all generated near the Tejo Plateau and moved into directions between  $210^\circ$  and  $260^\circ$ . The authors particularly describe one meddy pathway together with the dynamic topography at the beginning and the end of the experiment. The initially predominantly westward propagation is characterized by adjustment processes from bipolar to monopolar state that is followed by southwestward translation. The dipolar structure in the initial phase of the meddy formation process is particularly important, because it obviously prevents meddies from a reentrainment into the boundary current by following meanders. In the model experiment those meddies with a relatively strong dipolar characteristic in the beginning were able to escape through the western boundary of the model grid. The slight onshore movement of the first meddy described in [Fig. 11a](#)  that occurred between day 88 and 172 is probably due to the eastward directed flow on the upstream side of the cyclonic circulation region in the wake of the first shedding event.

#### 4. Sensitivity studies

Various authors ([Ambar and Howe 1979](#); [Prater and Sanford 1994](#); [Käse and Zenk 1996](#), among others) have suggested that the presence of canyons and ridges could have an important impact on the stability of the Mediterranean Undercurrent and on the formation of meddies. In the “canyon” experiment (cf. [Fig. 1b](#) ) a depression and in the “ridge” experiment an elevation (cf. [Fig. 1c](#) ) are introduced onto the otherwise linearly sloping topography. Both depth anomalies are of Gaussian shape in the alongslope direction, and the amplitude is maximum (300 m) at the shelf break and decreases linearly toward the bottom of the ocean. The horizontal extend at middepth is about 50 km. Since this is larger than the internal Rossby radius ( $\approx 10 \text{ km}$ ), the bottom flow will be able to follow the lateral excursion of the isobaths to conserve potential vorticity. Therefore, in addition to thickness variation as the bottom current overflows the obstacle, the effect of horizontal curvature of the topography comes into play. In a horizontal plane, therefore, the flow across a ridge (canyon) resembles the flow along a cape (bay). The curvature effect may lead to flow separation or blocking ([Røed 1980](#)). Lack of computer time prevented us from running the case studies over the full length of the standard experiment. However, deviations from the case described in [section 3](#) became visible early in the simulation. [Figure 12](#)  shows a blowup of the intermediate depth (1150 m) salinity field for both cases after 64 days of simulation. The figures should be compared with [Fig. 10a](#) .



the same region as displayed for the standard experiment at the same instant of time. The lateral injection at middepth shows that the shedding process is more advanced in both the canyon (Fig. 12a) and the ridge (Fig. 12b) case [note that Figs. 12a,b show some resemblance with the evolution of the anomaly in the standard experiment after 82 days (Fig. 10c)]. To demonstrate how the canyon and the ridge enhance the offshore displacement of the outflow water, we depict the relative vorticity field at 1150 m from a region centered at the topographic features in Fig. 13. The boundary current flowing from right to left into the figure possesses horizontal shear. Relative vorticity is negative shoreward of the center (minimum value about  $-0.3f$ ) and positive offshore. A relatively strong maximum of cyclonic vorticity is visible directly in the center of the canyon. Although the velocity vectors tend to follow the isobaths, the outflow layer is apparently stretched as it moves over the deeper trench. At the downstream side of the canyon there is a patch of anticyclonic vorticity as the flow climbs back on the linear slope. The vorticity induced by this mechanism enhances the offshore transport downstream of the axis of the canyon. This can be seen in Fig. 12a at  $x = -90$  km,  $y = -340$  km, where the velocity vectors are directed nearly westward and are not aligned to the topography. The effect is an offslope transport of saline water as is visible in the excursion of the 36.8 isohaline near the northern exit of the canyon. In the ridge case, there is a region of anticyclonic vorticity directly over the crest where the outflow layer is compressed. One would expect that this leads to a more clockwise deviation of the flow. However, another effect seems to be more important. An inspection of the velocity vectors and the 36.5-psu isohaline close to the boundary (Fig. 12b) reveals that the flow becomes narrower on the southern side of the ridge and is therefore accelerated (Røed 1980). At the tip of the ridge the current partly overshoots and separates horizontally from the lateral boundary. South of the ridge, there is a maximum of cyclonic vorticity. This is probably caused by the effect of outflowing water being ejected laterally into a region of smaller ambient vorticity so that it has to gain cyclonic vorticity. Downstream of the ridge there is a high salinity tongue ( $S > 36.8$  psu) seeming to be emanated from the tip of the ridge. The vorticity extrema associated with the canyon and the ridge are stationary and are not shed from the obstacles. In both cases, however, the topographic irregularities disturb the alignment of the boundary current with the slope so that it is more likely to be advected offshore by the mechanism described with the standard experiment. This corroborates earlier assumptions that horizontal shear, created at canyons and capes, might enhance the instability of the undercurrent. These features would also tend to restrict or localize the generation of meddies to certain geographical points, and there is some evidence for this in the observations. Trajectories of floats released in the undercurrent at the Portuguese continental slope north of Cape St. Vincent showed that nearly all meddies were spawned from the slope at the Tejo Plateau (Zenk et al. 1992), whereas floats seeded in the outflow water in the western Gulf of Cadiz (southeast of Cape St. Vincent) became unstable near a canyon in the region south of Portugal and were shed from the boundary at Cape St. Vincent where the coastline turns north at almost a right angle (Bower et al. 1995, 1997).

We also tested the sensitivity of the model to a variation of the bottom slope. The results are summarized qualitatively as follows. In the standard experiment, the inclination was set to  $s = 1.25 \times 10^{-2}$ . This represents a mean value of the slopes that are experienced by the Mediterranean outflow. However, between Gibraltar Strait and, say, the Tejo Plateau, the inclination of the bottom varies considerably. When the bottom slope was doubled, the boundary current was faster and the salinity anomaly was lower, owing to more intense vertical mixing. Shedding events were more energetic and resulted preferentially in dipoles that escaped through the western boundary of the model. In the case of a more gentle slope ( $s = 6.25 \times 10^{-3}$ ) the acceleration due to gravity was smaller initially. There was less entrainment during the initial adjustment phase on the continental slope and the plume retained its character as a bottom-arrested boundary current and the formation of intermediate depth meanders or detached dipoles were absent. However, at the downslope edge of the bottom water tongue, the front was meandering resembling the perturbed dense bottom plume of Jiang and Garwood (1996). Applying these findings to the Mediterranean outflow, the conclusion is that meddies are more likely to be formed to the south and west of Portugal where the bottom slope is much larger than in the eastern Gulf of Cadiz. Instability theory, on the other hand, suggest that a sloping bottom stabilizes the flow, similar to the planetary  $\beta$  effect (e.g., Pedlosky 1964). Swaters (1991) found a crucial dependence of the instabilities on a so-called interaction parameter  $\mu$ . This parameter, basically the plume height divided by the bottom slope, measures the ratio of the destabilizing effect of baroclinic vortex stretching/compression (as the plume moves through the slope water) to the stabilizing effect of the bottom slope that acts as a topographic  $\beta$  plane. In the present model setting, changing the bottom slope has, however, more than one effect. If the slope is increased, the effective downslope acceleration due to gravity  $g' \sin \alpha$  becomes larger resulting in higher velocities. Higher velocities (i.e., velocity shear across the interface) causes, in return, more mixing and the entrainment of lighter ambient water into the plume. This reduces  $g'$  (Price and Baringer 1994; Jungclauss and Backhaus 1994) and counteracts the initial effect. In the end, there is increased alongslope transport of more diluted water. Reducing the slope has, of course, the opposite effect. Thus, the stabilizing effect of increasing the ambient (topographic) vorticity gradient is apparently overwhelmed by the effect of enhanced vertical shear and reduced density anomaly.

## 5. Summary and discussion

The dense outflow simulated here was shown to be prone to instability in the previous sections. The wavelike structure and the vertical phase relations of the perturbations indicate that the instability is predominantly baroclinic. The lateral intrusions are associated with a transfer of potential energy from the mean flow into the perturbation potential energy that is then transformed into perturbation kinetic energy by the adjustment process. As the perturbations grow to large amplitudes, dipoles are formed initially and move offshore. Outflow water is advected into the interior introducing a lens-shaped deformation of the ambient isopycnals at middepth. This density structure supports anticyclonic circulation so that the

anticyclone amplifies the initial development, while the cyclone entrains ambient water, weakening its density anomaly. In those cases where the eddies separated, they showed meridional propagation of opposite direction, which is consistent with theories of dipoles and monopoles in the presence of an ambient vorticity gradient. It was shown that the lateral intrusion of the lens into the ambient compresses the water column above and below, so that anticyclonic vorticity is introduced to conserve potential vorticity. The meddies that show a velocity maximum of about  $15 \text{ cm s}^{-1}$  possess, therefore, a barotropic velocity component of a few centimeters per second. It was demonstrated that the low potential vorticity of the meddy stems from the Mediterranean outflow where it was created by frictional effects.

Although there is strong evidence of a baroclinic nature of the instability, we have seen that the outflow possess horizontal shear, and we cannot rule out a barotropic contribution. [Griffiths and Linden \(1981\)](#) stressed that barotropic processes significantly influence the wavelength of the fastest growing mode if  $h/H < 0.1$ , where  $h$  and  $H$  are the heights of the plume and the ambient water layer, respectively. In our case,  $h/H$  is about 0.15–0.2, not far from this threshold so that barotropic influences could be important. To quantify the different contributions to the instability process, it would be useful to set up an experiment that considers a dense filament on a sloping bottom in a periodic channel. This would enable us to calculate alongslope means and perturbations of the flow and to carry out a detailed energy analysis. Other open question relate to the representation of the meddy-induced lateral salt and heat transport in large-scale ocean models where they must be parameterized as eddy-driven horizontal or isopycnal diffusivity. To specify this diffusivity and its anisotropy (caused by the self propagation of the meddies) it would be useful to evaluate “meddy-resolving” models of the southeastern North Atlantic.

### Acknowledgments

I wish to thank George Mellor for his support and encouragement during my postdoctoral affiliation with the AOS program. Critical comments of the anonymous reviewers are gratefully acknowledged. Funding for this study was provided by the National Atmospheric and Oceanic Administration (NOAA) Grant NA67RJ0120. During the revision of the paper I received financial support by the German Ministry of Science and Technology (BMBF, WOCE IV).

---

### REFERENCES

- Ambar, I., and M. R. Howe, 1979: Observations of the Mediterranean outflow—II. The deep circulation in the vicinity of the Gulf of Cadiz. *Deep-Sea Res.*, **26**, 535–554..
- Arhan, M., and B. King, 1995: Lateral mixing of Mediterranean Water in the eastern North Atlantic. *J. Mar. Res.*, **53**, 865–895..
- Armi, L., and W. Zenk, 1984: Large lenses of highly saline Mediterranean water. *J. Phys. Oceanogr.*, **14**, 1560–1576.. [Find this article online](#)
- , D. Hebert, N. Oakey, J. Price, P. L. Richardson, T. Rossby, and B. Ruddick, 1989: Two years in the life of a Mediterranean salt lens. *J. Phys. Oceanogr.*, **19**, 354–370.. [Find this article online](#)
- Baey, J.-M., D. Renouard, and G. Chabert D’Hieres, 1995: Preliminary results about the stability of an intermediate water current. *Deep-Sea Res.*, **42**, 2063–2073..
- Baringer, M. O., 1993: Mixing and dynamics of the Mediterranean outflow. Ph.D. thesis, Massachusetts Institute of Technology/Woods Hole Oceanographic Institution Joint Program, WHOI-93-52, 244 pp. [Available from Woods Hole Oceanographic Institution, Woods Hole, MA 12543.].
- Beckmann, A., and R. H. Käse, 1989: Numerical simulations of the movements of a Mediterranean water lens. *Geophys. Res. Lett.*, **16**, 65–68..
- Blumberg, A. F., and G. L. Mellor, 1987: A description of a three-dimensional coastal ocean circulation model. *Three-Dimensional Coastal Ocean Models*, N. Heaps, Ed., Coastal Estuarine Sciences, Vol. 4, Amer. Geophys. Union, 1–16..
- Bower, A. S., L. Armi, and I. Ambar, 1995: Direct evidence of meddy formation off the southwestern coast of Portugal. *Deep-Sea Res.*, **42**, 1621–1630..
- , —, and —, 1997: Lagrangian observations of meddy formation during a Mediterranean undercurrent seeding experiment. *J. Phys. Oceanogr.*, **27**, 2545–2575.. [Find this article online](#)
- Chapman, D. C., 1985: Numerical treatment of cross-shelf open boundaries in a barotropic coastal ocean model. *J. Phys. Oceanogr.*, **15**, 1060–1075.. [Find this article online](#)
- Daniault, N., J. P. Mazé, and M. Arhan, 1994: Circulation and mixing of Mediterranean water west of the Iberian peninsula. *Deep-Sea*

D'Asaro, E. A., 1988: Generation of submesoscale vortices: A new mechanism. *J. Geophys. Res.*, **93**, 6685–6693..

Ezer, T., and G. L. Weatherly, 1990: A numerical study of the interaction between a deep cold jet and the bottom boundary layer of the ocean. *J. Phys. Oceanogr.*, **20**, 801–816.. [Find this article online](#)

Gill, A. E., 1981: Homogeneous intrusions in a rotating stratified fluid. *J. Fluid Mech.*, **103**, 275–295..

—, 1982: *Atmosphere–Ocean Dynamics*. Academic Press, 662 pp..

Griffiths, R. W., and P. F. Linden, 1981: The stability of buoyancy-driven coastal currents. *Dyn. Atmos. Oceans*, **5**, 281–306..

—, P. D. Killworth, and M. E. Stern, 1982: Ageostrophic instabilities of ocean currents. *J. Fluid Mech.*, **117**, 343–377..

Jiang, L., and R. W. Garwood Jr., 1996: Three-dimensional simulations of overflows on continental slopes. *J. Phys. Oceanogr.*, **26**, 1214–1233.. [Find this article online](#)

Johnson, G. C., T. B. Sanford, and M. O. Baringer, 1994: Stress on the Mediterranean outflow plume: Part I. Velocity and water property measurements. *J. Phys. Oceanogr.*, **24**, 2072–2083.. [Find this article online](#)

Jungclauss, J. H., and J. O. Backhaus, 1994: Application of a transient reduced gravity plume model to the Denmark Strait overflow. *J. Geophys. Res.*, **99**, 12 375–12 396..

—, and G. L. Mellor, 1999: A three-dimensional model study of the Mediterranean outflow. *J. Mar. Syst.*, in press..

Karsten, R. H., G. E. Swaters, and R. E. Thomson, 1995: Stability characteristics of deep water replacement in the Strait of Georgia. *J. Phys. Oceanogr.*, **25**, 2391–2403.. [Find this article online](#)

Käse, R. H., and W. Zenk, 1987: Reconstructed Mediterranean salt lens trajectories. *J. Phys. Oceanogr.*, **17**, 158–163.. [Find this article online](#)

—, and —, 1996: Structure of the Mediterranean Water and meddy characteristics in the northeastern Atlantic. *The Warmwatersphere of the North Atlantic Ocean*, W. Krauss, Ed., Gebrüder Bornträger Verlag, 365–395..

—, A. Beckmann, and H. H. Hinrichsen, 1989: Observational evidence of salt lens formation in the Iberian basin. *J. Geophys. Res.*, **94**, 4905–4912..

Kinder, T. B., and H. L. Bryden, 1990: Aspiration of deep waters through straits. *The Physical Oceanography of Sea Straits*, L. J. Pratt, Ed., Kluwer Academic Publishers, 295–313..

MacCready, P., and P. Rhines, 1993: Buoyant inhibition of Ekman transport on a slope. *J. Phys. Oceanogr.*, **23**, 5–22.. [Find this article online](#)

McWilliams, J. C., and P. R. Gent, 1986: The evolution of sub-mesoscale, coherent vortices on the  $\beta$ -plane. *Geophys. Astrophys. Fluid Dyn.*, **35**, 235–255..

Mellor, G. L., and T. Yamada, 1982: Development of a turbulence closure model for geophysical fluid problems. *Rev. Geophys. Space Phys.*, **20**, 851–875..

—, and A. F. Blumberg, 1985: Modeling vertical and horizontal diffusivities with the sigma-coordinate system. *Mon. Wea. Rev.*, **113**, 1380–1383.. [Find this article online](#)

Pedlosky, J., 1964: The stability of currents in the atmosphere and in the oceans. Part I. *J. Atmos. Sci.*, **21**, 201–219.. [Find this article online](#)

Prater, M. D., 1992: Observations and hypothesized generation of a meddy in the Gulf of Cadiz. Ph.D. thesis, University of Washington, 143 pp. [Available from Applied Physics Laboratory, University of Washington, Seattle, WA 98105-6698].

—, and T. B. Sanford, 1994: A meddy off Cape St. Vincent. Part I: Description. *J. Phys. Oceanogr.*, **24**, 1572–1586.. [Find this article online](#)

Price, J. F., and M. O. Baringer, 1994: Outflow and deep water production by marginal seas. *Progress in Oceanography*, Vol. 33, Pergamon, 161–200..

Røed, L. P., 1980: Curvature effects on hydraulically driven inertial boundary currents. *J. Fluid Mech.*, **96**, 395–412..

Schultz Tokos, K., and T. Rossby, 1991: Kinematics and dynamics of a Mediterranean salt lens. *J. Phys. Oceanogr.*, **21**, 879–892.. [Find this article online](#)

Shapiro, G. I., S. L. Meschanov, and M. V. Emelianov, 1995: Mediterranean salt lens ‘Irving’ after ist collision with seamounts. *Oceanol. Acta*, **18**, 309–318..

Siedler, G., W. Zenk, and W. J. Emery, 1985: Strong-current events related to a subtropical front in the Northeast Atlantic. *J. Phys. Oceanogr.*, **15**, 885–897.. [Find this article online](#)

Smagorinsky, J., 1963: General circulation experiments with the primitive equations. I. The basic experiment. *Mon. Wea. Rev.*, **91**, 99–164.. [Find this article online](#)

Stammer, D., H.-H. Hinrichsen, and R. H. Käse, 1991: Can Meddies be detected by satellite altimetry? *J. Geophys. Res.*, **96**, 7005–7014..

Swaters, G. E., 1991: On the baroclinic instability of cold-core coupled density fronts on a sloping continental shelf. *J. Fluid Mech.*, **224**, 361–382..

Wheatherly, G. L., and P. J. Martin, 1978: On the structure and dynamics of the oceanic bottom boundary layer. *J. Phys. Oceanogr.*, **8**, 557–570.. [Find this article online](#)

Zenk, W., 1975: On the Mediterranean outflow west of Gibraltar. *Meteor Forschungsergeb.*, **A16**, 23–34..

—, and L. Armi, 1990: The complex spreading patterns of Mediterranean Water off the Portuguese continental slope. *Deep-Sea Res.*, **37**, 1805–1823..

—, K. Schultz Tokos, and O. Boebel, 1992: New observations of meddy movement south of the Tejo plateau. *Geophys. Res. Lett.*, **19**, 2389–2392..

---

## APPENDIX

### 6. Potential Vorticity

Following [Prater and Sanford \(1994\)](#), we derive an expression for the potential vorticity in Cartesian coordinates. Ertel’s potential vorticity (PV)

$$Q = -(f\mathbf{k} + \zeta) \cdot \frac{\nabla\rho}{\rho}$$

is conserved following fluid parcels in the absence of frictional and viscous forces. Assuming thermal wind balance, the PV can be written

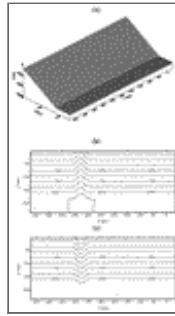
$$Q = -\frac{1}{\rho}(f + \zeta)\frac{\partial\rho}{\partial z} - \frac{f}{g}\left[\left(\frac{\partial u}{\partial z}\right)^2 + \left(\frac{\partial v}{\partial z}\right)^2\right].$$

The local density is given by  $\rho = \rho_M(z) + \rho'(x, y, z)$ , where  $\rho_M$  is the background density of the initial state when there was no outflow present, and  $\rho'$  is the density anomaly. Introducing background and perturbation buoyancy frequencies  $N_M$  and  $N'$ , respectively, the PV can be expressed in terms of nondimensional parameters

$$Q = Q_M[1 + \text{Ro} + G + \text{Ro}G - F],$$

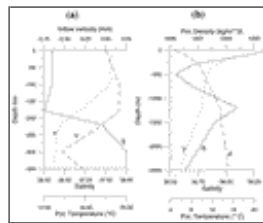
where  $Q_M$  is the mean PV  $fN_M^2/g$ ,  $\text{Ro}$  is a Rossby number  $\zeta/f$ ,  $G$  is the buoyancy anomaly term  $N'^2/N_M^2$ , and  $F$  is a Froude number  $[(\partial v/\partial z)^2 + (\partial u/\partial z)^2]/N_M^2$ . Since the model dynamics include friction and diffusivity, the relation is only approximately valid. However, it reflects effects of frictional dynamics, such as vertical shear in the bottom boundary layer, and serves as a convenient diagnostic tool. The equation is evaluated on  $\sigma$  levels, taking into account the appropriate correction terms.

## Figures



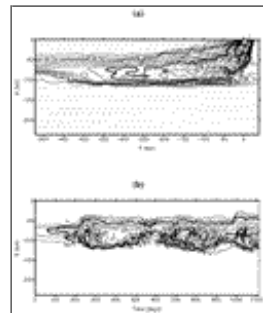
[Click on thumbnail for full-sized image.](#)

Fig. 1. Bottom topographies used with the numerical experiments; (a) perspective view of the idealized continental slope situated at the eastern boundary of an ocean; isobaths (c.i. = 250 m) of the topographies used with (b) the “canyon” and (c) the “ridge” experiment. The origin of the horizontal coordinates is located at the center of the inflow channel at the eastern boundary. The actual model domain (not shown) is extended by 10 grid points with gradually varying grid size to the north, south, and west.



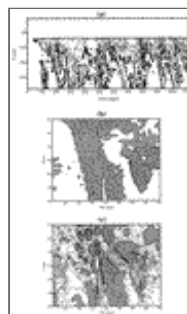
[Click on thumbnail for full-sized image.](#)

Fig. 2. Inflow and initial conditions; (a) vertical profiles of salinity (solid line), temperature (dotted line), and normal velocity (dashed line) applied at the inflow–outflow channel at the eastern boundary; (b) vertical profiles of salinity (solid line), temperature (dotted line), and potential density ( $\sigma_\theta$ ) (dashed line) used as initial conditions for the entire model domain.



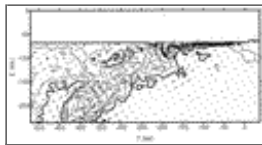
[Click on thumbnail for full-sized image.](#)

Fig. 3. The near-bottom ( $\sigma$ -level 28) salinity; (a) the horizontal field (c.i. = 0.1 psu) after 320 days of simulation; (b) a space–time plot taken at  $y = -350$  km. In (a) also the near-bottom velocity field (every fourth vector, max vector =  $0.9 \text{ m s}^{-1}$ ) is depicted.



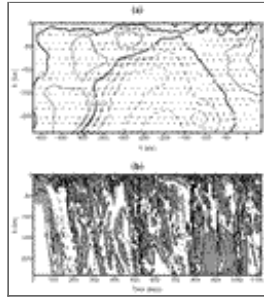
[Click on thumbnail for full-sized image.](#)

Fig. 4. Space–time plots of (a), (b) salinity (c.i. = 0.2 psu) on the 1150-m depth level and (c) relative vorticity (normalized by  $f$ , c.i. = 0.05). In (b) and (c) only a limited domain is displayed. In (a) the heavy contour line indicates the  $S = 36.3$  isohaline, and in (b) areas where  $S > 36.3$  are shaded. In (c) negative relative vorticities ( $\zeta < -0.05f$ ) are shaded and positive vorticities ( $\zeta > 0.05f$ ) are cross-hatched.



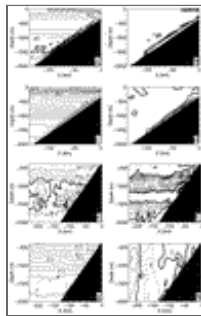
[Click on thumbnail for full-sized image.](#)

Fig. 5. The salinity (c.i. = 0.1 psu) and velocity (every fourth vector, max vector =  $0.2 \text{ m s}^{-1}$ ) field at 1150-m depth after 360 days of simulation. The boundary of the Mediterranean outflow water is indicated by the 36.3 isohaline (heavy contour line).



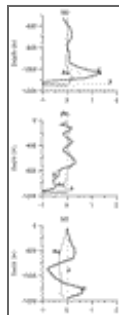
[Click on thumbnail for full-sized image.](#)

Fig. 6. The near-surface flow regime, (a) sea surface height (c.i. = 1 cm) and velocity field (every fourth vector, max vector =  $0.1 \text{ m s}^{-1}$ ) at  $z = 20 \text{ m}$ ; (b) space–time plot of the near-surface relative vorticity normalized by  $f$  (c.i. = 0.1). Negative vorticities ( $\zeta > 0.05f$ ) are shaded and positive values ( $\zeta > 0.05f$ ) are cross-hatched.



[Click on thumbnail for full-sized image.](#)

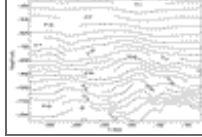
Fig. 7. Cross-slope transects at (a)–(d)  $y = -100 \text{ km}$ , and (e)–(h)  $y = -395 \text{ km}$ . (a), (e) Salinity (c.i. = 0.1 psu), the 36.3 isohaline is highlighted by the heavy contour. (b), (f), Potential vorticity normalized by the potential vorticity of the undisturbed field (c.i. = 0.1, only regions where the potential vorticity is reduced are displayed). (c), (g) Potential density (c.i. =  $0.1 \text{ kg m}^{-3}$ ). (d), (h) Alongslope velocity [c.i. =  $10 \text{ cm s}^{-1}$ , dashed lines indicate negative (southward) flow].



[Click on thumbnail for full-sized image.](#)

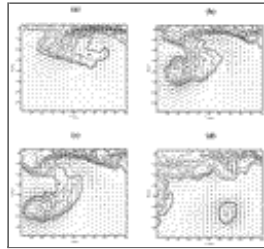
Fig. 8. Profiles of the dimensionless terms contributing to the potential vorticity anomaly at (a)  $x = -67 \text{ km}$ ,  $y = -100 \text{ km}$ , (b)  $x = -67 \text{ km}$ ,  $y = -320 \text{ km}$ , and (c)  $x = -195 \text{ km}$ ,  $y = -395 \text{ km}$ . Rossby number  $Ro$  (thin line), buoyancy anomaly  $G$  (solid line), and Froude number  $F$  (dashed line).





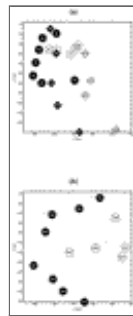
Click on thumbnail for full-sized image.

Fig. 9. Meridional section (parallel to the coast) at  $x = -67$  km; (a) cross-shore velocity [c.i. =  $3 \text{ cm s}^{-1}$ , negative (westward) velocities dashed], and (b) potential density (c.i. =  $0.05 \text{ kg m}^{-3}$ ).



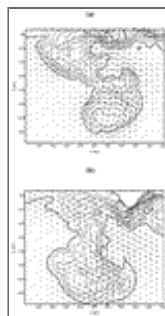
Click on thumbnail for full-sized image.

Fig. 10. Evolution of a singular lens. Salinity (c.i. =  $0.1 \text{ psu}$ ) and velocity vectors (max vector =  $15 \text{ cm s}^{-1}$ ) from a limited domain at  $t =$  (a) 64, (b) 72, (c) 82, and (d) 172 days.



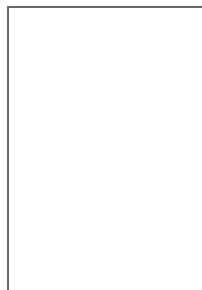
Click on thumbnail for full-sized image.

Fig. 11. Pathways of selected anticyclones (filled symbols) and cyclones (open symbols). Numbers indicate model days. The displayed area include the “outer” model domain where zonal grid size and horizontal friction are increased; (a) the event displayed in [Fig. 10](#) (dots) together with a dipole that did not break off into isolated vortices (squares), (b) propagation and separation of another vortex pair.



Click on thumbnail for full-sized image.

Fig. 12. Salinity (c.i. =  $0.1 \text{ psu}$ ) and velocity field at 1150-m depth from a limited domain after 64 days of simulation for the case of (a) a canyon and (b) a ridge superimposed onto the otherwise linear slope. The boundary of the Mediterranean outflow water is indicated by the 36.3 isohaline (heavy contour line).



  
Click on thumbnail for full-sized image.

Fig. 13. Relative vorticity normalized by  $f$  after 64 days of simulation for a limited domain centered around the topographic irregularities; (a) canyon and (b) ridge case.

\* Current affiliation: Max-Planck-Institut für Meteorologie, Hamburg, Germany.

*Corresponding author address:* Dr. Johann H. Jungclaus, Max-Planck-Institut für Meteorologie, Bundesstrasse 55, 20146 Hamburg, Germany.

E-mail: [jungclaus@dkrz.de](mailto:jungclaus@dkrz.de)

top ▲



© 2008 American Meteorological Society [Privacy Policy and Disclaimer](#)

Headquarters: 45 Beacon Street Boston, MA 02108-3693

DC Office: 1120 G Street, NW, Suite 800 Washington DC, 20005-3826

[amsinfo@ametsoc.org](mailto:amsinfo@ametsoc.org) Phone: 617-227-2425 Fax: 617-742-8718

[Allen Press, Inc.](#) assists in the online publication of *AMS* journals.